Wang *et al. Catal* (2026) 2:4
https://doi.org/10.1007/s44422-026-00018-w

Catal

ARTICLE Open Access

Site-selective Ru doping in spinel Co_3O_4 unlocks dual-site synergy for acidic water electrolysis

Yumeng Wang[1], Yaling Zhang[1], Shiyao Chen[1], Yameng Fan[2], Jian Peng[3], Tofik Ahmed Shifa[4], Yaping Li[1*], Alberto Vomiero[4], Fengmei Wang[1*] and Xiaoming Sun[1*]

Abstract

The development of stable, efficient, and low-cost catalysts for the oxygen evolution reaction (OER) in acidic media, along with a deeper understanding of the underlying reaction mechanisms, remains a central focus in the field of acidic water electrolysis. Herein, catalysts were strategically designed to selectively substitute octahedral and tetrahedral Co sites in Co_3O_4 with Ru to figure out the role of metal site in different coordination environments for acidic OER activity and stability. By regulating the synthesis strategy and tailoring the crystal coordination environment, we achieved Oct-$Ru_xCo_{3-x}O_4$ and Tet-$Ru_xCo_{3-x}O_4$ samples with selective substitution of Ru at octahedral and tetrahedral sites in Co_3O_4. Experimental and theoretical analysis confirm that Ru substitution at octahedral Co^{3+} sites activates a dual-metal Ru_{oct}-O-Co_{oct} active center through the oxide path mechanism (OPM) with a reduced energy barrier, whereas tetrahedral substitution disrupts orbital overlap due to excessive atomic spacing. The electron transfer within the Ru_{oct}-O-Co_{oct} configuration effectively suppresses cobalt over-oxidation and dissolution. Consequently, the octahedrally substituted Oct-$Ru_{0.13}Co_{2.87}O_4$ catalyst with only 4 at% Ru exhibits moderate yet promising acidic OER performance, requiring a low overpotential of 240 mV and demonstrating stable operation for over 240 h at 10 mA cm^{-2}. This performance notably surpasses that of the tetrahedral substituted counterpart, which requires a higher overpotential of 280 mV and sustains stability for only 42 h. This work provides new insights into site-selective substitution strategies in spinel oxides, and establishes a paradigm for designing cost-effective non-precious metal-based catalysts for hydrogen production.

Keywords Ruthenium-doped Co_3O_4, Selective substitution, Acidic oxygen evolution reaction, Spinel structure, PEM water electrolysis

*Correspondence:
Yaping Li
liyp@mail.buct.edu.cn
Fengmei Wang
wangfm@buct.edu.cn
Xiaoming Sun
sunxm@mail.buct.edu.cn

[1]State Key Laboratory of Chemical Resource Engineering, College of Chemistry, Beijing University of Chemical Technology, Beijing 100029, P. R. China
[2]School of Science, RMIT University, Melbourne, VIC 3000, Australia
[3]Eastern Institute for Advanced Study, Eastern Institute of Technology, Ningbo 315200, China
[4]Department of Molecular Sciences and Nanosystems, Ca' Foscari University of Venice, Via Torino 155, Venezia Mestre 30172, Italy

Springer

Introduction

The gradual depletion of conventional energy resources such as coal and petroleum necessitates a transition to clean energy alternatives to drive sustainable energy transformation and environmental preservation [1]. Green hydrogen, produced via renewable energy-powered water electrolysis, has emerged as a promising solution due to its carbon neutrality and high energy density [2, 3]. Among the various water electrolysis technologies, proton exchange membrane water electrolysis (PEMWE) stands out for its enhanced safety, high current density, high-purity hydrogen production, superior energy efficiency, and compact design compared to alkaline systems [4, 5]. However, its commercialization remains hindered by the high operational costs associated with significant energy losses caused by the large overpotential of the anodic oxygen evolution reaction (OER), which requires elevated cell voltages. The absence of cost effective catalysts that simultaneously deliver satisfactory activity and durability remains a critical bottleneck for acidic water electrolysis [6]. Constrained by the harsh acidic conditions, only a few materials exhibit both sufficient activity and long-term stability. As a result, PEMWE currently relies heavily on noble metals (particularly Ir [7, 8] and Ru [9, 10] based materials), significantly increasing overall system costs. For instance, Ir-based oxides exhibit exceptional stability in acidic media due to the high oxidation potential required to dissolve Ir species (IrO_x) [11]. Nevertheless, the scarcity and exorbitant cost of Ir severely restrict its industrial scalability. Ru-based catalysts, with higher intrinsic activity and lower cost, tends to oxidize into soluble RuO_4 species, at anodic potentials above 1.4 V vs. RHE, leading to rapid degradation and compromised long-term durability [12, 13]. This limitation demand the urgent need to explore cost-effective, earth-abundant alternatives that can deliver both high activity and stability in acidic media. In response, increasing efforts have been devoted to developing non-noble metal catalysts such as Co_3O_4, [14] MnO_2, [15] TiO_2, [16] Nb_2O_5, [17] CeO_2 [18] for acidic OER. Despite promising advancements, achieving sufficient durability and catalytic efficiency remains a significant challenge, primarily due to the corrosive nature of the acidic medium and the high anodic potentials. Maintaining structural integrity and catalytic performance under strongly acidic conditions remains a critical challenge for these alternative materials. Moreover, the unfavorable adsorption energies of some non-noble metal elements for OER intermediates lead to heightened activation energy barriers, thereby limiting their catalytic activity. Among the emerging candidates, cobalt oxide (Co_3O_4) has attracted copious attention as a promising transition metal oxide catalyst, owing to its abundance, relative stability, and interesting redox properties [19, 20]. Nonetheless, its performance in acidic conditions remains unsatisfactory, primarily due to limited intrinsic activity and susceptibility to degradation. To address these limitations, heteroatom doping has proven effective in modulating the electronic structure and introducing additional active sites for OER [21, 22]. Particularly, the incorporation of noble metal elements can modulate the electronic structure of Co_3O_4, mitigate their over oxidation and subsequent dissolution, and ultimately extend the operational lifespan in acidic media. In order to have a successful doping, it is important to understand the chemical role therein.

Typically, Co_3O_4 is spinel oxides, with the general formula AB_2O_4 crystallize in a closely packed cubic Fd3m symmetry, where A-site cations (Co^{2+}) occupy tetrahedral positions and B-site cations (Co^{3+}) reside in octahedral sites. The octahedral Co^{3+} sites exhibit strong σ-σ interactions with oxygen, while tetrahedral Co^{2+} sites display weaker π-π interactions [23, 24]. A particularly valuable aspect of spinel-type Co_3O_4 emanates from the ability to clearly distinguish the catalytic roles of each cobalt site and selectively introduce foreign atoms into targeted lattice positions [25]. The specific role of each site can be assessed by selectively substituting Co^{2+} or Co^{3+} with other elements. For instance, in studies related to the hydrogen evolution reaction (HER), Zn replaces tetrahedral Co^{2+} as in $ZnCo_2O_4$, where it shows comparable activity to pristine Co_3O_4. While, Al replaces octahedral Co^{3+} as in $CoAl_2O_4$, demonstrates significantly reduced activity [26]. However, this approach cannot directly reveal the intrinsic activity differences between cobalt atoms in the two coordination environments since the findings are influenced by the specific activity of the substituting ions. Recent studies propose that Co_3O_4 may enable a dual-site oxide path mechanism (OPM) during OER, where synergistic interactions between tetrahedral and octahedral sites facilitate direct O-O coupling [27]. This pathway circumvents the thermodynamic limitations of the conventional adsorbate evolution mechanism (AEM), which involves sequential *OH→*OOH transitions, and avoids structural collapse caused by lattice oxygen vacancies in the lattice oxygen mechanism (LOM) [28]. The role of crystallographic site-selective substitution in modulating the competition between lattice oxygen participation and adsorbate evolution remains elusive, particularly in dictating the thermodynamic and kinetic feasibility of O-O coupling pathways. In acidic media, the Co^{3+}/Co^{4+} redox couple activated near 1.6 V vs. RHE is critical for OER activity [29]. However, over-oxidation of Co^{3+} to unstable CoO_2 at high potentials severely compromises durability [21, 30, 31]. The strategic incorporation of foreign metals into Co_3O_4 provides a promising avenue for tailoring spinel oxides to acidic water electrolysis, potentially suppressing over-oxidation and enhancing OER activity [32].

Herein, we employ controlled ruthenium substitution at distinct crystallographic sites to probe the site dependent OER activity and stability. The site-selective Ru incorporation was verified by Raman spectra and extended X-ray absorption fine structure (EXAFS) spectra analyses. The incorporation of Ru was found to significantly enhance both the OER activity and structural stability of Co_3O_4. Notably, Ru substitution at octahedral sites, denoted as Oct-$Ru_xCo_{3-x}O_4$, demonstrated superior stability compared to tetrahedral substitution. The synergistic interactions between Ru_{oct} and Co_{oct} sites shortens the Ru_{oct}-O-Co_{oct} bond length, facilitating direct *O-*O coupling via the OPM pathway. This pathway effectively circumvents the rate-limiting *OOH intermediate formation inherent to the AEM pathway, enabling Oct-$Ru_{0.13}Co_{2.87}O_4$ electrode to achieve 10 mA cm^{-} [2] at a low overpotential of 240 mV, respectively. Octahedral substitution with equivalent ruthenium loading delivers markedly enhanced activity and stability relative to the tetrahedral analogues of Tet-$Ru_{0.18}Co_{2.82}O_4$ with almost the same Ru ratio, which demonstrates the overpotential of 260 mV at 10 mA cm^{-} [2]. Concurrently, Oct-$Ru_{0.13}Co_{2.87}O_4$ electrode could operate stably for over 240 h at 10 mA cm^{-} [2] with a low decay rate of only 0.6 mV h^{-} [1], in contrast to Tet-$Ru_{0.18}Co_{2.82}O_4$ which exhibits a significant and rapidly voltage surge within 50 h. The enhanced stability is attributed to facile electron transfer through Ru-O-Co bonding networks, which mitigates oxidative dissolution of Co species and stabilizes the spinel lattice. These findings unveil a viable strategy to engineer non-noble metal oxides as high performance acidic OER catalysts, highlighting the critical role of rational crystallographic site modulation in optimizing both activity and operational durability.

Results and discussions

Characterization of Oct/Tet-$Ru_xCo_{3-x}O_4$

To build the Oct/Tet-$Ru_xCo_{3-x}O_4$ crystal models, we firstly use the same ratio of Ru to replace different chemical coordinated Co sites in spinel Co_3O_4 crystal. And then we investigated the stability of these crystal models by calculating the dissolution energy required for Ru and Co sites (Fig. 1a). We found that although the dissolution energy for Co is similar with the value of 4.50 eV the dissolution energy of Ru at octahedral site (6.07 eV) is much higher than that at tetrahedral site (3.22 eV). This suggests the formation of octahedral Ru site is much more stable. Then, samples with Ru partially substituting Co at either tetrahedral or octahedral sites in Co_3O_4 were synthesized by the different preparation routes shown in Fig. 1b. Undoped Co_3O_4 was used as a reference to evaluate their performance differences in acidic water electrolysis. The atomic ratios of Ru and Co in prepared catalysts were determined by inductively coupled plasma optical emission spectrometry (ICP-OES, Table S1-2). Based on the metal atomic ratios, the samples were designated as Oct-$Ru_xCo_{3-x}O_4$ (x = 0.08, 0.13, 0.47, 0.59) and Tet-$Ru_xCo_{3-x}O_4$ (x = 0.07, 0.18, 0.42). Scanning electron microscopy (SEM) images of Oct-$Ru_xCo_{3-x}O_4$ and Tet-$Ru_xCo_{3-x}O_4$ samples show the flower-like nanosheet structures regularly aligned on the carbon fiber surface, similar with the Co_3O_4 sample (Fig. 1c-f and Fig S1-3). The interconnected pores observed between the nanosheets of Oct-$Ru_xCo_{3-x}O_4$ and Tet-$Ru_xCo_{3-x}O_4$ are known to facilitate the transportation of oxygen. High-resolution transmission electron microscopy (HR-TEM, Fig. 1g-h and Fig S4) confirms that both Oct-$Ru_xCo_{3-x}O_4$ and Tet-$Ru_xCo_{3-x}O_4$ show similar lattice spacings to Co_3O_4 with (311) and (200) crystal planes. Specifically, Oct-$Ru_{0.13}Co_{2.87}O_4$ shows a slight increase in lattice spacing compared to Tet-$Ru_{0.18}Co_{2.82}O_4$, in which the spacing distance increases from 0.247 nm to 0.256 nm for (311) crystal plane, possibly due to more pronounced lattice expansion caused by Ru incorporation into the more sterically constrained octahedral sites. The XRD patterns of both Oct-Rux$Co_{3-x}O_4$ and Tet-$Ru_xCo_{3-x}O_4$ in Fig. 1i-j closely matches the standard spinel Co_3O_4 phase (JCPDS no. 74-2120), with no detectable impurity peaks other than a carbon peak at 25°, confirming that Ru doping preserves the Co_3O_4 crystal structure. Furthermore, the energy dispersive X-ray spectroscopy (EDX) mapping of Oct-$Ru_xCo_{3-x}O_4$ and Tet-$Ru_xCo_{3-x}O_4$ demonstrates homogeneous distribution of Ru, Co, and O, with Ru signals overlapping precisely with Co and O (Fig. 1k and Fig S5-S8). Overall, these results collectively indicate that Ru atoms are successfully incorporated into the Co_3O_4 lattice rather than forming surface RuO_2 clusters on the Co_3O_4 nanosheet surfaces.

Electronic Structure Characterizations of Oct/Tet-$Ru_xCo_{3-x}O_4$

. To confirm the site selective substitution of Ru in Co_3O_4, Raman spectroscopy was performed and the results is shown in Figs. 2a-b. Pristine Co_3O_4 exhibits five characteristic vibrational modes: three F_{2g} modes, E_g mode, and A_{1g} mode. The E_g mode is caused by the symmetrical bending vibration of O in the lattice, leading to stretching or elongation of the Co-O bond, and exists throughout the entire lattice. The A_{1g} mode correspond to the symmetric stretching of Co^{3+}-O in the octahedral units, while the F_{2g} modes are attributed to the vibrational coupling of Co^{2+}-O in the tetrahedral units [33, 34]. Both Oct-$Ru_xCo_{3-x}O_4$ and Tet-$Ru_xCo_{3-x}O_4$ retain Raman profiles similar to Co_3O_4, with distinct peak shifts toward lower wavenumbers, indicative of lattice strain induced by the doping of a lager radius atom. Notably, Oct-$Ru_xCo_{3-x}O_4$ shows a more pronounced redshift in the A_{1g} (~ 6 cm^{-} [1]) and E_g (~ 6 cm^{-} [1]) modes compared to the F_{2g} [1] modes

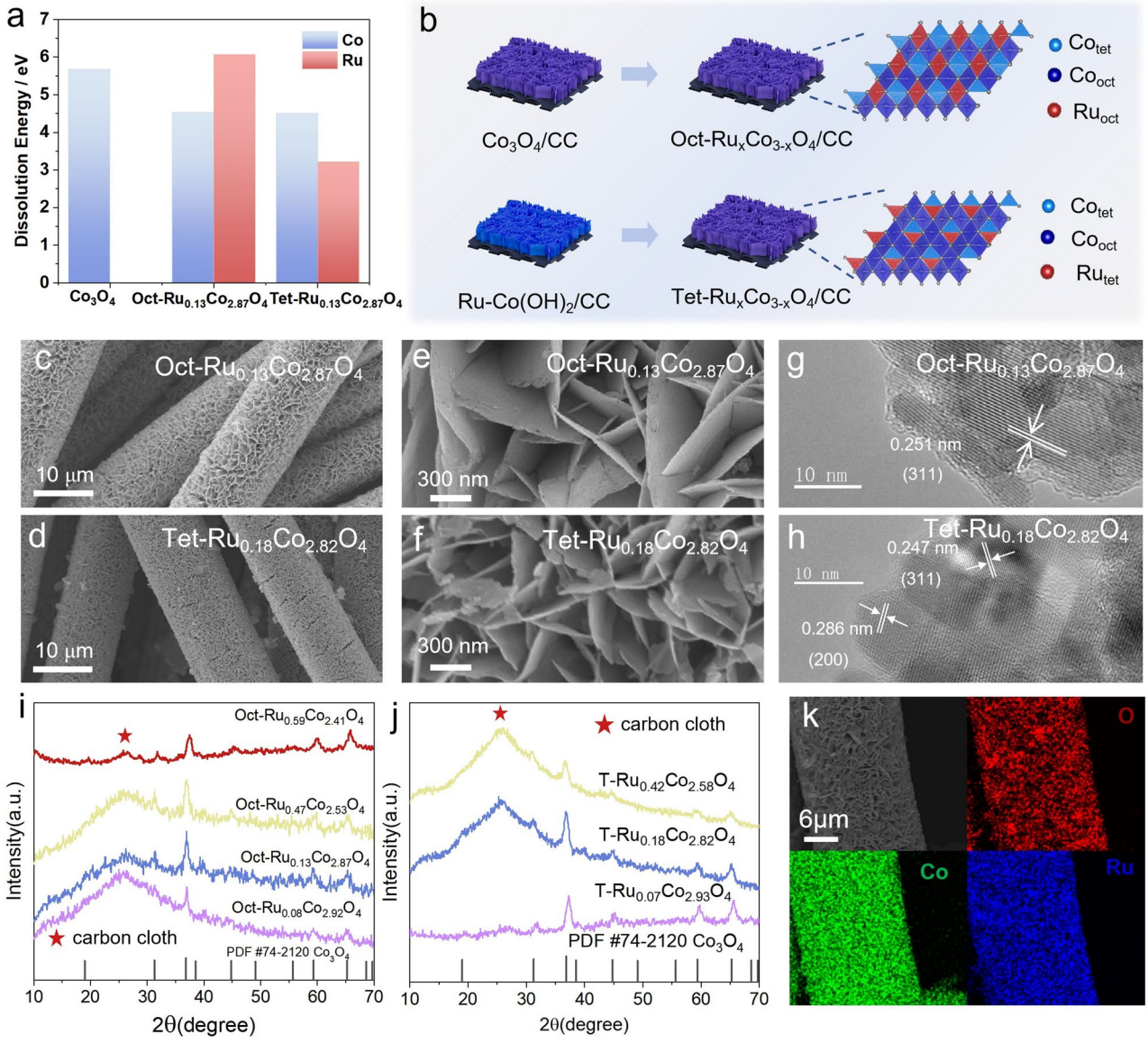

Fig. 1 (**a**) Calculated dissolution energy values for Co and Ru ions from Oct-$Ru_{0.13}Co_{2.87}O_4$, Tet-$Ru_{0.13}Co_{2.87}O_4$ and Co_3O_4 models. (**b**) Schematic illustration of the synthetic process for different catalysts. SEM images of (**c**, **e**) Oct-$Ru_{0.13}Co_{2.87}O_4$ and (**d**, **f**) Tet-$Ru_{0.18}Co_{2.82}O_4$ samples on carbon cloth. HR-TEM images of (**g**) Oct-$Ru_{0.13}Co_{2.87}O_4$ and (**h**) Tet-$Ru_{0.18}Co_{2.82}O_4$ sample. XRD spectra of (**i**) Oct-$Ru_xCo_{3-x}O_4$, (**j**) Tet-$Ru_xCo_{3-x}O_4$. (**k**) the EDS mapping of Oct-$Ru_{0.13}Co_{2.87}O_4$

(~ 2 cm^{-1}), whereas Tet-$Ru_xCo_{3-x}O_4$ exhibits a stronger redshift in the F_{2g} [1] mode (~ 3 cm^{-1} for F_{2g} [1] vs. 1.5 cm^{-1} for A_{1g}). This contrast confirms that Ru preferentially occupies octahedral sites during ion exchange process but substitutes tetrahedral sites in electrodeposited catalysts, probably influenced by the applied potential during deposition.

X-ray photoelectron spectroscopy (XPS) was employed to investigate the electronic interactions between Ru and Co in Oct-$Ru_{0.13}Co_{2.87}O_4$ and Tet-$Ru_{0.18}Co_{2.82}O_4$ as representative samples. The Co 2*p* spectra of Oct-$Ru_{0.13}Co_{2.87}O_4$ and Tet-$Ru_{0.18}Co_{2.82}O_4$ display binding energy upshifts relative to pristine Co_3O_4 (Fig. 2c and Fig S8-10) [35, 36]. Specifically, Oct-$Ru_{0.13}Co_{2.87}O_4$ shows a moderate reduction (0.1 eV), while Tet-$Ru_{0.18}Co_{2.82}O_4$ exhibits a more significant shift (0.3 eV). This electronic modulation arises from electron transfer from Ru to Co via bridging oxygen atoms, effectively lowering the oxidation state of Co. The stronger shift in Tet-$Ru_{0.18}Co_{2.82}O_4$ suggests enhanced electron redistribution when Ru occupies tetrahedral sites, likely due to their closer proximity to surface-active Co^{3+} species. The Co 2*p* XPS spectra of Oct-$Ru_{0.13}Co_{2.87}O_4$ and Tet-$Ru_{0.18}Co_{2.82}O_4$ exhibit distinct variations in the Co^{2+}/Co^{3+} ratio compared to that of pure Co_3O_4, due to Ru substitution at different crystallographic sites. The Co^{2+}/Co^{3+} ratios are 0.95 for

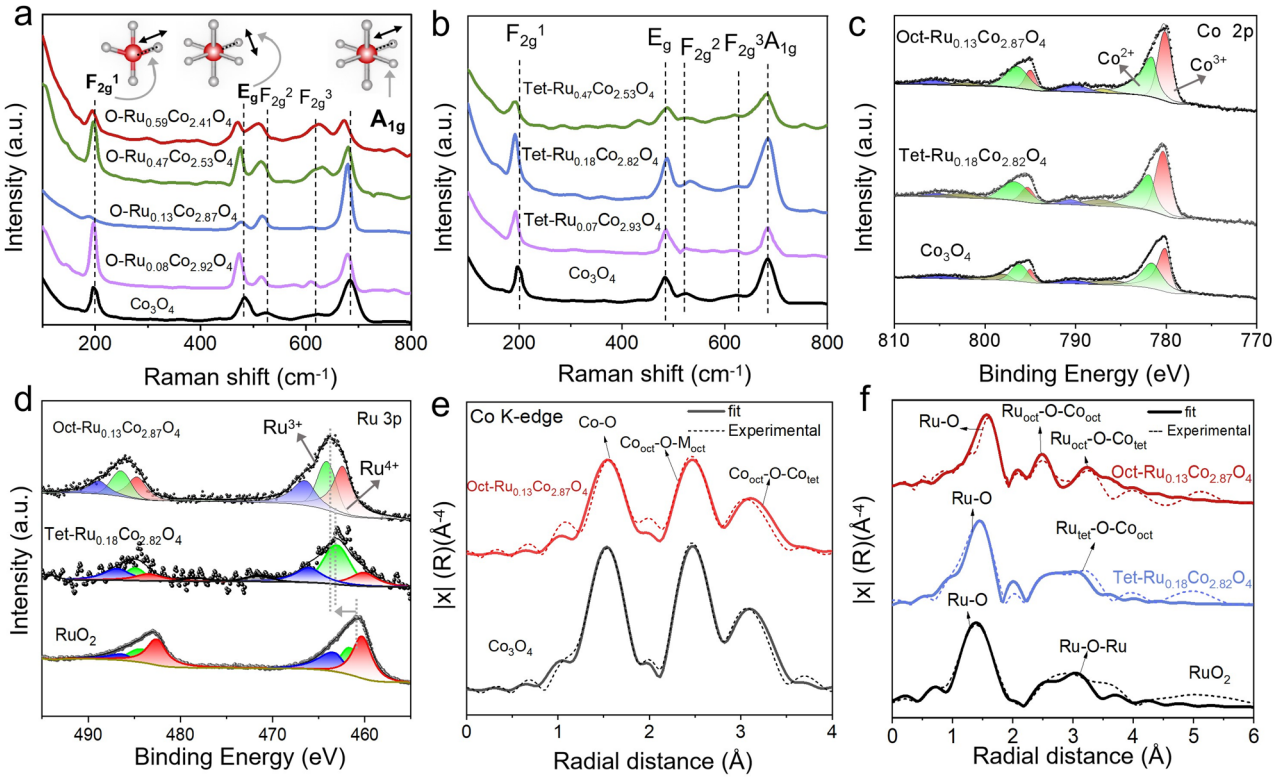

Fig. 2 Raman spectra of (**a**) Oct-$Ru_xCo_{3-x}O_4$ and (**b**) Tet-$Ru_xCo_{3-x}O_4$ samples with Co_3O_4 as reference. (**c**) Co 2*p* XPS spectra of Oct-$Ru_{0.13}Co_{2.87}O_4$, Tet-$Ru_{0.18}Co_{2.82}O_4$ and Co_3O_4. (**d**) Ru 3*p* XPS spectra of the Oct-$Ru_{0.13}Co_{2.87}O_4$, Tet-$Ru_{0.18}Co_{2.82}O_4$ and RuO_2. Fourier-transformed Co *K*-edge EXAFS spectra of Oct-$Ru_{0.13}Co_{2.87}O_4$ and Co_3O_4. (**f**) Fourier-transformed Ru *K*-edge EXAFS spectra of Oct-$Ru_{0.13}Co_{2.87}O_4$, Tet-$Ru_{0.18}Co_{2.82}O_4$ -samples compared with the RuO_2 reference

Oct-$Ru_{0.13}Co_{2.87}O_4$, 0.93 for Tet-$Ru_{0.18}Co_{2.82}O_4$, and 0.89 for undoped Co_3O_4. These results are consistent with the shift of Co 2*p* spectra, which may in turn influence both the electronic structure and the catalytic activity of the sample. Figure 2d shows the Ru 3*p* XPS spectra. Compared to that of RuO_2, the Ru 3*p* XPS spectra of Oct-$Ru_{0.13}Co_{2.87}O_4$ and Tet-$Ru_{0.18}Co_{2.82}O_4$, which have almost same elemental ratios with different crystal site substitution, exhibit a decreased overall binding energy, implying the lower oxidation state of Ru in the Oct-$Ru_{0.13}Co_{2.87}O_4$ and Tet-$Ru_{0.18}Co_{2.82}O_4$ catalyst. The variation in binding energy shift originates from the different substitution sites of Ru in Co_3O_4, depending on whether it occupies octahedral or tetrahedral Co sites. To further solidify these findings, X-ray absorption spectroscopy including X-ray absorption near edge structure (XANES) and extended X-ray absorption fine structure (EXAFS) was carried out to further investigate the effect of Ru doping on the electronic structures of Co and Ru in Oct/Tet-$Ru_xCo_{3-x}O_4$. Compared to Co_3O_4, the Co *K*-edge XANES spectra of Oct-$Ru_{0.13}Co_{2.87}O_4$ show a slight decrease in the valence state of Co induced by Ru-substitution (Fig S12). Additionally, the Ru *K*-edge XANES spectra demonstrate that Ru in Oct-$Ru_{0.13}Co_{2.87}O_4$ and Tet-$Ru_{0.18}Co_{2.82}O_4$ exhibits oxidation states between + 3 and + 4, higher than $RuCl_3$ but lower than RuO_2 (Fig S13). Notably, the Ru oxidation state in Oct-$Ru_{0.13}Co_{2.87}O_4$ is slightly reduced compared to Tet-$Ru_{0.18}Co_{2.82}O_4$, consistent with the Ru 3*p* XPS spectra results. The EXAFS analysis shows that the Co-O, Co_{oct}-Co_{oct}, and Co_{oct}-Co_{tet} path distances in O-$Ru_{0.13}Co_{2.87}O_4$ remain nearly identical to those in pristine Co_3O_4 (Fig. 2e). The soft XAS spectra of Co L-edge were conducted to confirm the valence state of Co. The binding energy of Oct-$Ru_{0.13}Co_{2.87}O_4$ sample has a red shift than pure Co_3O_4 sample, which is consistent with the XPS spectra analysis and indicating the substitution of Ru at octahedral Co site in spinel Co_3O_4. On the contrary, the binding energy of Tet-$Ru_{0.18}Co_{2.82}O_4$ sample has a opposite bule shift compared to pure Co_3O_4 sample due to the Ru substitution at Co^{2+} sites (Fig S14). Ru *K*-edge FT-EXAFS spectra reveal that the characteristic peak at 2.47 Å in the second shell of Oct-$Ru_{0.13}Co_{2.87}O_4$ (Fig. 2f, Fig S15) which can be assigned to Ru_{oct}–Co_{oct} coordination closely matching the Co_{oct}-Co_{oct} bond distance in pristine Co_3O_4 (2.46 Å). This evidences that the Ru substitution in Oct-$Ru_{0.13}Co_{2.87}O_4$ sample is indeed located at octahedral Co sites. The weaker FT peak at 3.21 Å in higher shells corresponds to Ru_{oct}-Co_{tet} coordination, which differs markedly from the Ru_{oct}-Ru_{oct} coordination in RuO_2 (3.05 Å).

This observation rules out the presence of pure RuO_2 phases in Oct-$Ru_{0.13}Co_{2.87}O_4$, which is consistent with XRD pattern analysis. For Tet-$Ru_{0.18}Co_{2.82}O_4$, the characteristic FT peak at 3.12 Å is assigned to Ru_{tet}-Co_{oct} coordination. The diminished peak intensity at 2.45–2.47 Å compared to Oct-$Ru_{0.13}Co_{2.87}O_4$ further indicates minimal Ru_{oct}-Co_{oct} bonding, validating the Raman spectroscopy findings that Ru predominantly occupies tetrahedral Co sites. There is also a remarkable elongation of the Ru–O bond length in both samples compared to standard RuO_2, as observed in Oct-$Ru_{0.13}Co_{2.87}O_4$ (1.57 Å vs. 1.40 Å in RuO_2) and Tet-$Ru_{0.18}Co_{2.82}O_4$ (1.45 Å vs. 1.40 Å, Fig. 2f). This elongation can be attributed to a reduction in the Ru valence state relative to that in RuO_2 and increases the electron density at the Ru vicinity for regulating the adsorption–desorption energetics of oxygen intermediates to facilitating the OER process.

Acidic OER activity of the Oct/Tet-$Ru_xCo_{3-x}O_4$

To evaluate the impact of Ru substitution at distinct crystallographic sites on acidic OER activity, the different electrodes with the same catalyst mass loading of ~ 2 mg cm^{-} [2] were tested in 0.5 M H_2SO_4 electrolyte. Polarization curves in Fig. 3a-b reveal that Oct-$Ru_xCo_{3-x}O_4$ and

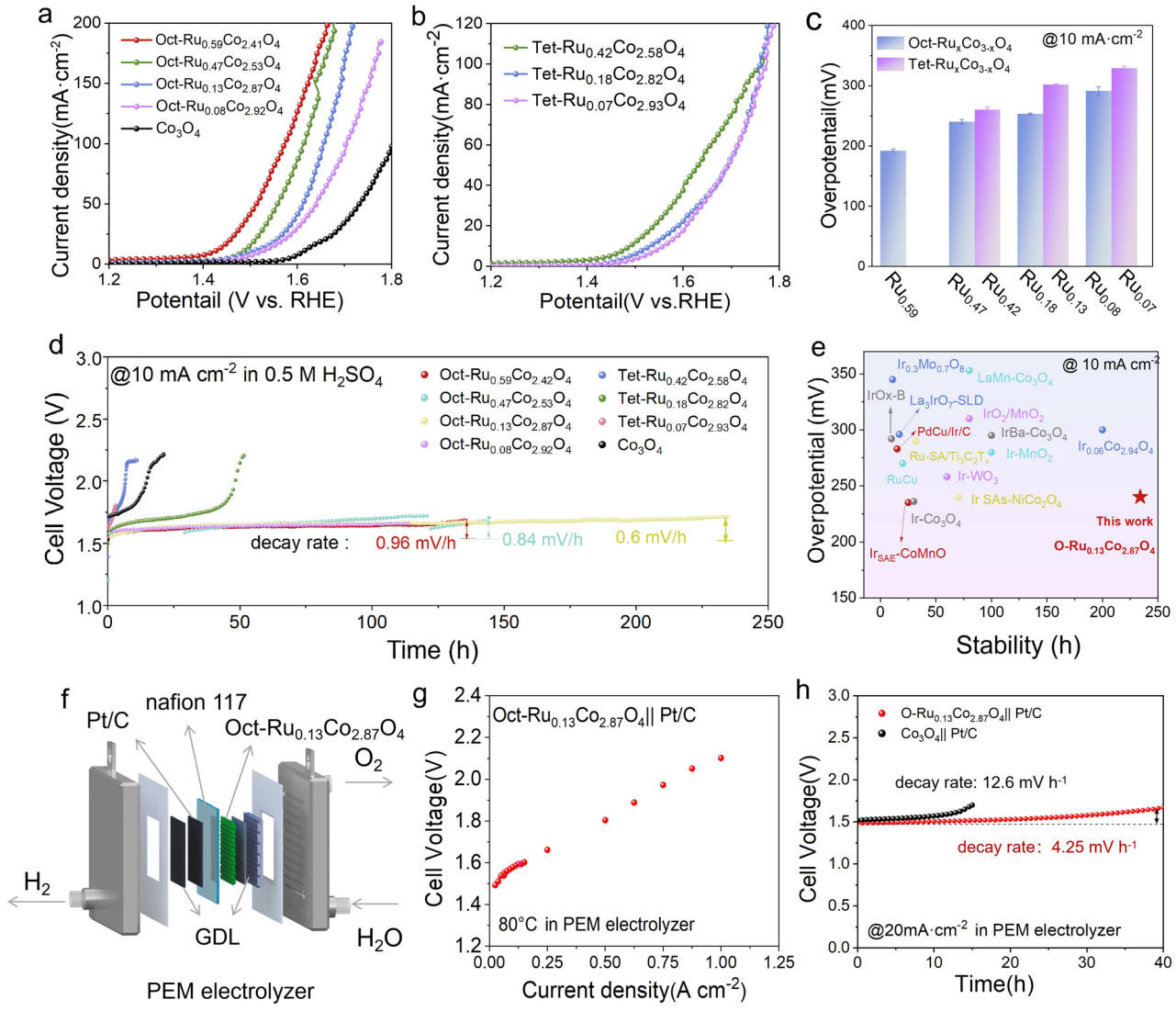

Fig. 3 (**a**) Polarization curves collected from various Oct-$Ru_xCo_{3-x}O_4$ electrodes, compared with the Co_3O_4 electrode. (**b**) Polarization curves collected from various Tet-$Ru_xCo_{3-x}O_4$ electrodes. (**c**) Overpotential at the current density of 10 mA cm^{-} [2] for various Oct-$Ru_xCo_{3-x}O_4$ and Tet-$Ru_xCo_{3-x}O_4$ electrodes. (**d**) Chronopotentiometry measurements of the Oct-$Ru_xCo_{3-x}O_4$ and Tet-$Ru_xCo_{3-x}O_4$ electrodes at 10 mA cm^{-} [2] in two-electrode cell with Pt plate as the cathode. The Co_3O_4 electrode is tested as a reference. (**e**) Comprehensive evaluation of overpotential and stability at 10 mA cm^{-} [2] for the Oct-$Ru_{0.13}Co_{2.87}O_4$ and other recently reported acidic OER electrocatalysts. (**f**) Schematic illustration of the fabricated PEM device with MEA electrode. (**g**) Steady-state polarization curves of Oct-$Ru_{0.13}Co_{2.87}O_4$ collected from PEM device with the size of 2 × 2 cm^2. (**h**) Chronopotentiometry curves of Oct-$Ru_{0.13}Co_{2.87}O_4$ and Co_3O_4 anodes tested on the PEM device at 20 mA cm^{-} [2]

Tet-$Ru_xCo_{3-x}O_4$ electrodes require significantly lower overpotentials than pristine Co_3O_4 to achieve identical current densities. The Oct-$Ru_{0.59}Co_{2.41}O_4$ electrode delivers 10 mA cm^{-2} at an overpotential of merely 192 mV, which is much lower than that for Co_3O_4 electrode (380 mV). Notably, Oct-$Ru_xCo_{3-x}O_4$ electrode consistently exhibits better activity to Tet-$Ru_xCo_{3-x}O_4$ electrode at equivalent Ru loadings (Fig. 3c), rationalized by the preferential substitution of Ru at octahedral Co^{3+} sites which are the primary active centers in spinel Co_3O_4. The Tafel slopes of Oct-$Ru_xCo_{3-x}O_4$ and Tet-$Ru_xCo_{3-x}O_4$ electrodes (Fig S16-17) were studied and compared. When Ru was introduced at octahedral sites, the Oct-$Ru_{0.13}Co_{2.53}O_4$ electrode demonstrates similar Tafel slope (128.4 mV dec^{-1}) with the tetrahedral site substituted counterpart of Tet-$Ru_{0.18}Co_{2.82}O_4$ (108.6 mV dec^{-1}) at the similar Ru ratio. This observation further suggests the same Volmer-Heyrovsky reaction mechanism on both electrodes. Next, the electrochemically active surface area (ECSA) was estimated by measuring the double-layer capacitance (C_{dl}) values for different electrodes. The results confirm that both the Oct-$Ru_{0.13}Co_{2.87}O_4$ (88.74 mF cm^{-2}) and Tet-$Ru_{0.18}Co_{2.82}O_4$ (42.91 mF cm^{-2}) exhibit higher ECSA than pristine Co_3O_4 (27.82 mF cm^{-2}, Figs S18-19). Then, we normalize LSV curves based on ECSA values of each electrode (Fig S20). The Oct-$Ru_xCo_{3-x}O_4$ electrodes show the better activity than the corresponding Tet-$Ru_xCo_{3-x}O_4$ ones with the same Ru ratio, demonstrating a same trend as the polarization curves in Fig. 3a and b. In particular, Oct-$Ru_{0.13}Co_{2.87}O_4$ achieves the higher ECSA, surpassing Tet-$Ru_{0.18}Co_{2.82}O_4$ at similar Ru loadings due to the much more exposed active sites. The electrochemical impedance spectroscopy (EIS) measurement conducted at 1.50 V vs. RHE demonstrates the smaller series resistance (R_s) for Oct-$Ru_{0.13}Co_{2.87}O_4$ (1.53 Ω) and Tet-$Ru_{0.18}Co_{2.82}O_4$ (1.63 Ω) electrodes than the pristine Co_3O_4 electrode (1.84 Ω) (Fig S21-22). Although the electron transfer resistance (R_{ct}) decreases with an increasing Ru ratio, the R_{ct} value for Oct-$Ru_{0.13}Co_{2.87}O_4$ and Tet-$Ru_{0.18}Co_{2.82}O_4$ electrodes remain around 3.17 and 3.5 Ω, respectively. This shows the enhanced electrochemical accessibility and density of active sites in the octahedrally substituted sample.

Beyond activity, stability is a critical metric for evaluating acidic OER catalysts. Next, we tested the stability of Oct-$Ru_xCo_{3-x}O_4$ and Tet-$Ru_xCo_{3-x}O_4$ electrodes, combined with Co_3O_4 electrode, through chronopotentiometry measurement at a current density of 10 mA cm^{-2}. The stability test at 10 mA cm^{-2} reveals rapid degradation for the pristine Co_3O_4 due to the oxidation of Co^{3+} to soluble Co^{4+} under high voltage (Fig. 3d). It is noted that Oct-$Ru_{0.13}Co_{2.87}O_4$ exhibited the longest stable operation time of 240 h, featuring the smallest decay rate of only 0.6 mV h^{-1} at 10 mA cm^{-2}. Such activity and stability represent a significant advantage over previously reported non-precious metal-based acidic OER catalysts (Fig. 3e). Nevertheless, Tet-$Ru_xCo_{3-x}O_4$ (x = 0.18, 0.42) electrodes exhibits a rapid voltage increase within 50 and 20 h under constant current testing, comparable to pure Co_3O_4. This implies possible instability of Ru in the tetrahedral sites, with potential dissolution or phase separation at high potentials. Subsequently, XRD characterization was performed on the Tet-$Ru_{0.18}Co_{2.82}O_4$ sample after 50 h stability test at 10 mA cm^{-2}, revealing the emergence of a RuO_2 crystalline phase (JCPDS card no. 43-1027, Fig S23). And the Raman spectra also show the specific peak of RuO_2 (E_g, A_{1g} and B_{2g} peaks) but no characteristic vibrational modes for Co_3O_4 phase, which could indicate the unstable structure of the catalyst (Fig S24). The XRD spectra of Oct-$Ru_{0.13}Co_{2.87}O_4$ and Oct-$Ru_{0.59}Co_{2.41}O_4$ after stability test at 10 mA cm^{-2} for 240 h and 125 h shows the disappearance of cobalt oxide and RuO_2 crystal phase due to the existence of the amorphous phase after long-term stability test (Fig S25). The Raman spectra collected from Oct-$Ru_{0.13}Co_{2.87}O_4$ and Oct-$Ru_{0.59}Co_{2.41}O_4$ electrode after stability test in Fig S26 verify the maintenance of catalyst. There are no new Raman peaks in Oct-$Ru_xCo_{3-x}O_4$ (x = 0.13 and 0.59) even after prolonged stability test, highlighting the promising stability of Ru in the octahedral sites of Co_3O_4. The XPS spectra of Oct-$Ru_{0.13}Co_{2.87}O_4$ sample after 240 h stability test at 10 mA cm^{-2} was collected in Fig S27. Compared with the fresh sample, the valance states of Ru and Co elements in the Oct-$Ru_{0.13}Co_{2.87}O_4$ after stability test are increased due to the oxidation during OER process. The free energy required for dissolution Ru_{oct} site was 6.07 eV, which is much higher than that (3.22 eV) for Ru_{tet} site, further confirming the higher stability of Ru atoms at the octahedral Co site of the Co_3O_4. The SEM image and EDS analysis of Oct-$Ru_{0.13}Co_{2.87}O_4$ sample after the stability test at 10 mA cm^{-2} for 240 h is conducted and shown in Fig S28. The result shows that the atomic ratio of Ru: Co (0.13: 2.87) is still close to that value (0.12 : 2.88) in the fresh sample, indicating the compositional stability of Ru.

To assess the industrial applicability of the most active electrocatalyst (Oct-$Ru_{0.13}Co_{2.87}O_4$), we constructed a 2 × 2 cm^2 PEM water electrolyzer (PEMWE) employing the synthesized catalysts on the anode and 20 wt% Pt/C on the cathode (Fig. 3f). This PEMWE device requires a cell voltage of 1.66 V to deliver a current density of 250 mA cm^{-2} (Fig. 3g). And it can be stably operated at 20 mA cm^{-2} for over 30 h, exhibiting a low voltage decay rate of 4.25 mV h^{-1} (Fig. 3h), much better than that for the Co_3O_4 anode (12.6 mV/h). Notably, a remarkably low noble metal loading of only 0.15 mg cm^{-2} was demonstrated in this PEMWE device, elucidating the catalyst's

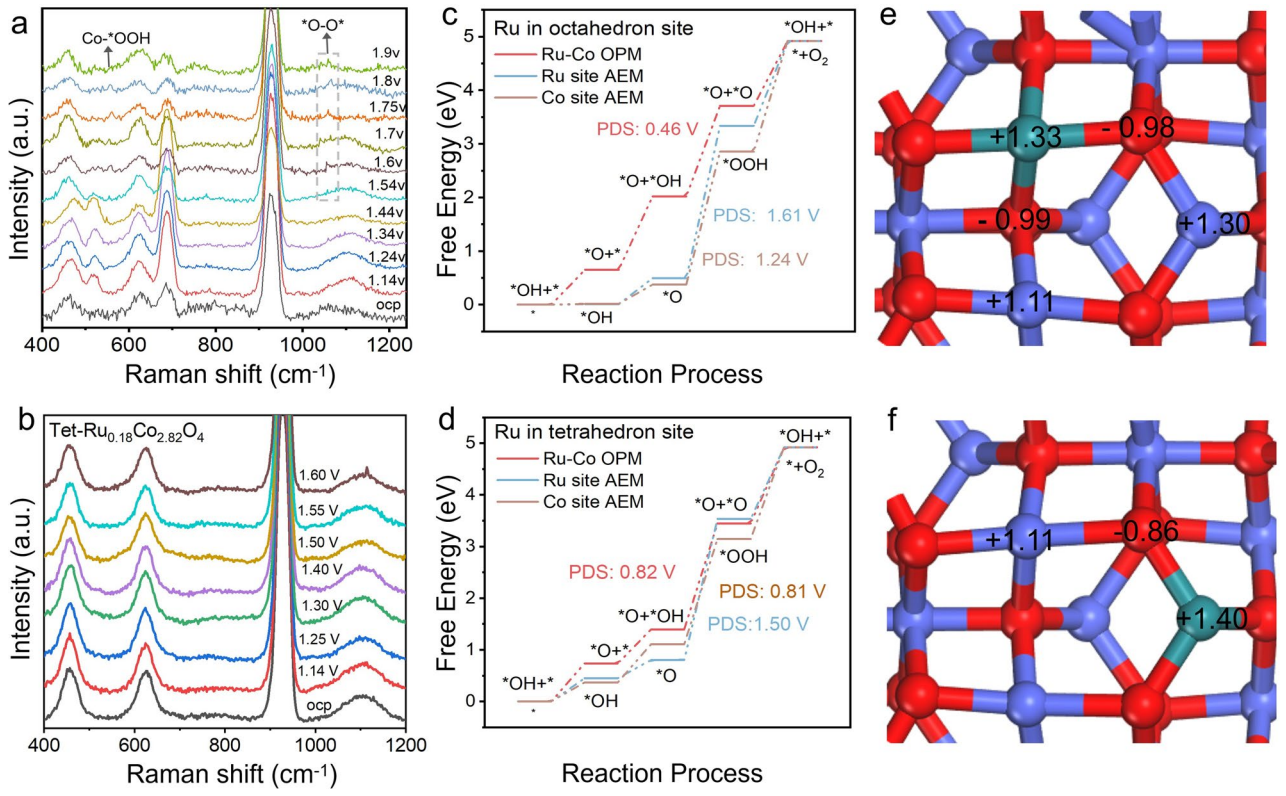

Fig. 4 In-situ Raman spectra collected from (**a**) Oct-$Ru_{0.13}Co_{2.87}O_4$ and (**b**) Tet- $Ru_{0.18}Co_{2.82}O_4$ electrode under different potentials. Gibbs free energy diagrams of (**c**) Oct-$Ru_{0.13}Co_{2.87}O_4$ and (**d**) Tet-$Ru_{0.13}Co_{2.87}O_4$ based on OPM and AEM pathway. Bader charge distribution diagrams of (**e**) Oct-$Ru_{0.13}Co_{2.87}O_4$, and (**f**) Tet-$Ru_{0.13}Co_{2.87}O_4$

promising potential for cost-effective and scalable hydrogen production technologies.

The OER reaction mechanism on Oct-$Ru_xCo_{3-x}O_4$and Tet-$Ru_xCo_{3-x}O_4$catalysts

To gain in-depth insights into the nature of active sites and electrocatalytic mechanism during OER process, two routes were pursued: (i) In-situ Raman measurements were conducted at the working electrode from open circuit potential (OCP) to 1.9 V vs. RHE in 0.1 M $HClO_4$, providing real-time information on the electronic and structural changes of the catalyst under operating conditions. (ii) Theoretical calculations were performed on the optimized surface to elucidate the reaction pathways and the energy barriers for the intermediate species. Both approaches provided profound insights into the nature of the active sites, offering valuable clues about the underlying catalytic mechanism and the key factors contributing to the enhanced activity. Considering that Raman spectroscopy could capture various intermediates during the OER, [37] we performed in-situ Raman spectrum tests on Oct-$Ru_{0.13}Co_{2.87}O_4$ and Tet-$Ru_{0.18}Co_{2.82}O_4$ in 0.1 M $HClO_4$ electrolyte (Fig. 4a and b). For Oct-$Ru_{0.13}Co_{2.87}O_4$, the Raman peak observed at ~ 560 cm^{-} [1] beyond 1.45 V vs. RHE can be assigned to the CoOOH intermediate species formed after Co oxidation [38, 39]. This observation aligns with prior studies demonstrating that high-valent $Co^{>+3}$ species are generated in spinel Co_3O_4 prior to the OER, which act as active centers to facilitate *O-*O bond formation. The Raman peak observed at ~ 1080 cm^{-} [1] under potentials exceeding 1.6 V vs. RHE can be attributed to the *O-*O intermediate species characteristic of the oxide path mechanism (OPM) [21]. These spectral features indicate that Co undergoes oxidation to high-valent species prior to OER, while the activated Ru-Co dual sites facilitate direct *O-*O coupling during the reaction. This observation corroborates the synergistic role of Ru-O-Co coordination in enabling the OPM pathway, bypassing the conventional adsorbate evolution steps. In contrast, such Raman modes are not observed from the in-situ Raman spectra collected from Tet-$Ru_{0.18}Co_{2.82}O_4$ electrode (Fig. 4b) possibly because Ru substitution at tetrahedral Co sites fails to activate the dual-site OER process, evidencing the importance of site-specific Ru incorporation.

Next, DFT calculations were further carried out to elucidate the mechanistic differences induced by site-selective Ru substitution. Models with identical Ru content (4 at%) were constructed with Ru occupying octahedral and tetrahedral sites. The Gibbs free energies associated

with the adsorbate evolution mechanism (AEM) pathway at different Ru and Co sites, as well as those corresponding to the OPM pathway involving cooperative interactions between Ru_{oct}-O-Co_{oct} are depicted in Fig. 4c and d. For Oct-$Ru_{0.13}Co_{2.87}O_4$ model, the potential- determining step (PDS) following AEM pathway is the *O→*OOH step at Ru and Co sites (1.61 eV and 1.24 eV, respectively). Although the PDS at Ru sites following AEM pathway is more energetically demanding than at Co sites, the dehydrogenation of *OH and O_2 desorption are significantly facilitated, suggesting a synergistic OPM pathway involving Ru-Co dual sites to balance the energy barriers across reaction steps. The calculation obviously proves that the energy barrier of OER reaction via OPM mechanism on Ru-Co dual sites could be dramatically decreased to 0.46 eV. In contrast, for Tet-$Ru_{0.13}Co_{2.87}O_4$, the energy barrier of PDS step for the Ru_{tet}-O-Co_{oct} following OPM pathway increases to 0.82 eV, higher than the AEM pathway at Co_{oct} site (0.81 eV), due to the excessive Ru_{tet}-Co_{oct} distance (over 3Å) in the spinel lattice, which hinders effective orbital overlap. The shorter M_{oct}-Co_{oct} distance in Oct-$Ru_{0.13}Co_{2.87}O_4$ (2.79 Å), compared with Tet-$Ru_{0.13}Co_{2.87}O_4$ (2.89 Å) is key for triggering the OPM pathway at Ru_{oct}-Co_{oct} dual sites. The AEM pathway at Ru_{tet} site exhibits even higher barriers, confirming that tetrahedral substitution restricts intermediate adsorption, aligning with experimental observations. Moreover, the Bader charge was calculated to analyze the effect of Ru substitution on the coordination environment of Co_3O_4 (Fig. 4e, f and Fig S29). It reveals that Ru_{oct} substitution reduces the positive charge on adjacent Co_{oct} centers (+1.11 vs. +1.33 in pristine Co_3O_4) mitigating over-oxidation of Co site during the reaction and enhancing structural stability. Conversely, Ru_{tet} substitution increases the charge on neighboring Co_{oct} sites, larger than that in Oct-$Ru_{0.13}Co_{2.87}O_4$ (+1.12 vs. +1.11), suggesting the ease of over oxidation at high potential. Comparing with Ru_{oct} oxidation state (+1.33), Ru_{tet} site exhibits a higher positive charge (+1.4). In addition, the charge density difference analysis reveals distinct electronic redistributions in Oct-$Ru_{0.13}Co_{2.87}O_4$ and Tet-$Ru_{0.13}Co_{2.87}O_4$ compared to pristine Co_3O_4 (Fig S30). In Oct-$Ru_{0.13}Co_{2.87}O_4$, prominent electron accumulation is observed around Ru_{oct} atoms, accompanied by electron depletion at adjacent Co_{oct} sites, indicating directional electron transfer from Ru to Co through Ru-O-Co bridges. While, Tet-$Ru_{0.13}Co_{2.87}O_4$ shows local electron enrichment near the Ru_{tet} atom and the restrained electron transfer between Ru_{tet}-O-Co_{oct} due to the weak electronic coupling between the Ru_{tet} and Co_{oct} sites. This asymmetric charge redistribution, induced by site-selective Ru doping, is attributed to the stronger σ-σ overlap in octahedral coordination compared to the π-π dominated interactions in tetrahedral geometry. These theoretical calculation results further corroborate that Ru substitution at octahedral sites significantly modulates the Co_3O_4 electronic structure, whereas tetrahedral substitution imposes limited influence, aligning with the observed divergence in OER activity and stability. The projected density of states (PDOS) analysis reveals that Ru doping in both cases significantly modifies the electronic structure compared to pristine Co_3O_4. Specifically, Ru incorporation enhances the hybridization of electronic states near the Fermi level and reduces the bandgap thereby improving its intrinsic electronic conductivity (Fig S31) for accelerated electrochemical electron transfer. Additionally, the *d*-band centers of Co and Ru in Oct-$Ru_{0.13}Co_{2.87}O_4$ shift closer to the Fermi level (−1.35 eV) compared to Tet-$Ru_{0.13}Co_{2.87}O_4$, which is favorable for optimizing the adsorption energy of OER intermediates. In general, the DFT results mechanistically explain the experimentally observed activity differences between the Oct-$Ru_xCo_{3-x}O_4$ and Tet-$Ru_xCo_{3-x}O_4$ samples, highlighting the critical role of site-specific Ru substitution in modulating the electronic structure and catalytic behavior.

Conclusion

In summary, we achieved and validated the site-selective substitution of Ru in Co_3O_4 through systematic synthesis and characterizations, demonstrating that crystallographic site-selective Ru substitution in Co_3O_4 governs both OER activity and stability. The observed activity and stability findings confirm that Co^{3+} at octahedral sites serves as the intrinsic active center in spinel Co_3O_4. The superior activity of Oct-$Ru_xCo_{3-x}O_4$ is associated with optimized intermediate adsorption and enhanced electron transfer kinetics. The optimal Ru_{oct}-O-Co_{oct} interatomic distance triggers a dual-metal active site configuration, enabling OPM pathway with a reduced reaction barrier and enhanced OER activity. In contrast, tetrahedral substitution fails to activate synergistic pathways due to unfavorable atomic spacing. As a result, Oct-$Ru_{0.13}Co_{2.87}O_4$ can operate stably with suppressing over-oxidation of Co than the Tet-$Ru_{0.13}Co_{2.87}O_4$. This work not only delivers a high-performance acidic OER catalyst with minimal precious metal content but also establishes a rational design strategy for spinel oxides through site-selective substitution, providing atomic-level insights into the origin of site-dependent catalytic behavior.

Associated content

Supporting information

The Supporting Information has the Supplementary characterization and electrochemical test results of the catalysts, such as SEM images, XPS, EXAFS spectra, Tafel plots, CV curves and DFT calculations.

Supplementary Information

The online version contains supplementary material available at https://doi.org/10.1007/s44422-026-00018-w.

Supplementary Material 1.

Authors' contributions

Y.W., F.W. and X.S. conceived the project and designed the experiments. Y.W. conducted the experimental measurements. Y. Z. and Y.L. conducted the theoretical calculations. S.C. drew the PEM device picture. J.P. and Y.F. performed the XAS characterizations. Y.W., T.A.S., A.V., F.W. and X.S. wrote the manuscript with support from all authors.

Funding

This work was supported by National Key Research and development project (2023YFB4005100), National Natural Science Foundation of China (No. 22249005), Fundamental Research Funds for the Central Universities (buctrc202324), Young Elite Scientists Sponsorship Program by CAST (2023QNRC001) and the Young Elite Scientists Sponsorship Program by BAST (BYESS2023093).

Data availability

No datasets were generated or analysed during the current study.

Declarations

Competing interests

The authors declare no competing interests.

Received: 22 December 2025 / Revised: 14 January 2026 / Accepted: 16 January 2026
Published online: 04 February 2026

References

1. Chu S, Majumdar A (2012) Opportunities and challenges for a sustainable energy future. Nature 488:294–303. https://doi.org/10.1038/nature11475
2. Liu Z et al (2022) Challenges and opportunities for carbon neutrality in China. Nat Reviews Earth Environ 3:141–155. https://doi.org/10.1038/s43017-021-00244-x
3. Wang Y, Yan H, Fu H (2025) Recent advances and modulation tactics in Ru- and Ir-based electrocatalysts for PEMWE anodes at large current densities. *eScience* 5, 100323. https://doi.org/10.1016/j.esci.2024.100323
4. Wang CR et al (2025) Proton exchange membrane (PEM) water electrolysis: Cell-Level considerations for Gigawatt-Scale deployment. Chem Rev 125:1257–1302. https://doi.org/10.1021/acs.chemrev.3c00904
5. Xu Z, Wu Z-S (2025) Scalable production of high-performance electrocatalysts for electrochemical water splitting at large current densities. eScience 5:100334. https://doi.org/10.1016/j.esci.2024.100334
6. Du Y et al (2024) Design principle and regulation strategy of noble Metal-Based materials for practical proton exchange membrane water electrolyzer. Adv Energy Mater 15:2404113. https://doi.org/10.1002/aenm.202404113
7. Li A et al (2024) Atomically dispersed hexavalent iridium oxide from MnO2 reduction for oxygen evolution catalysis. Science 384:666–670. https://doi.org/10.1126/science.adg5193
8. Torrero J et al (2023) High performance and durable anode with 10-Fold reduction of iridium loading for proton exchange membrane water electrolysis. Adv Energy Mater 13:2204169. https://doi.org/10.1002/aenm.202204169
9. Yuan B et al (2025) Synergistic Niobium and manganese co-doping into RuO2 nanocrystal enables PEM water splitting under high current. Nat Commun 16:4583. https://doi.org/10.1038/s41467-025-59710-5
10. Liu H et al (2023) Eliminating over-oxidation of ruthenium oxides by Niobium for highly stable electrocatalytic oxygen evolution in acidic media. Joule 7:558–573. https://doi.org/10.1016/j.joule.2023.02.012
11. Jiang G et al (2021) Low-Loading and highly stable membrane electrode based on an Ir@WOxNR ordered array for PEM water electrolysis. ACS Appl Mater Interfaces 13:15073–15082. https://doi.org/10.1021/acsami.0c20791
12. Zhang J et al (2025) Tantalum-stabilized ruthenium oxide electrocatalysts for industrial water electrolysis. Science 387:48–55. https://doi.org/10.1126/science.ado9938
13. Zhao S et al (2025) Hydroxylation strategy enables Ru–Mn oxide for stable proton exchange membrane water electrolysis under 1 A cm−2. ACS Nano 19:8773–8785. https://doi.org/10.1021/acsnano.4c15900
14. Li D et al (2024) Isolated octahedral Pt-Induced electron transfer to Ultralow-Content Ruthenium-Doped spinel Co3O4 for enhanced acidic overall water splitting. J Am Chem Soc 146:28728–28738. https://doi.org/10.1021/jacs.4c07089
15. Lin C et al (2021) In-situ reconstructed Ru atom array on α-MnO2 with enhanced performance for acidic water oxidation. Nat Catal 4:1012–1023. https://doi.org/10.1038/s41929-021-00703-0
16. Li Y et al (2025) Integrating interactive Ir atoms into titanium oxide lattice for proton exchange membrane electrolysis. Adv Mater 37:2407386. https://doi.org/10.1002/adma.202407386
17. Shi Z et al (2022) Enhanced acidic water oxidation by dynamic migration of oxygen species at the Ir/Nb2O5 – x Catalyst/Support interfaces. Angew Chem Int Ed 61:e202212341. https://doi.org/10.1002/anie.202212341
18. Shi W et al (2025) Ultrastable supported oxygen evolution electrocatalyst formed by ripening-induced embedding. Science 387:791–796. https://doi.org/10.1126/science.adr3149
19. Zhang R et al (2023) Tracking the role of defect types in Co3O4 structural evolution and active motifs during oxygen evolution reaction. J Am Chem Soc 145:2271–2281. https://doi.org/10.1021/jacs.2c10515
20. Mondschein JS et al (2017) Crystalline Cobalt oxide films for sustained electrocatalytic oxygen evolution under strongly acidic conditions. Chem Mater 29:950–957. https://doi.org/10.1021/acs.chemmater.6b02879
21. Zhu W et al (2023) Direct dioxygen radical coupling driven by octahedral Ruthenium–Oxygen–Cobalt collaborative coordination for acidic oxygen evolution reaction. J Am Chem Soc 145:17995–18006. https://doi.org/10.1021/jacs.3c05556
22. Ko W et al (2025) Controlled structural activation of iridium single atom catalyst for High-Performance proton exchange membrane water electrolysis. J Am Chem Soc 147:2369–2379. https://doi.org/10.1021/jacs.4c11442
23. Zhou Y et al (2019) Significance of engineering the octahedral units to promote the oxygen evolution reaction of spinel oxides. Adv Mater 31:1902509. https://doi.org/10.1002/adma.201902509
24. Plaisance CP, van Santen RA (2015) Structure sensitivity of the oxygen evolution reaction catalyzed by Cobalt(II,III) oxide. J Am Chem Soc 137:14660–14672. https://doi.org/10.1021/jacs.5b07779
25. Dou Y et al (2016) Graphene-like Holey Co3O4 nanosheets as a highly efficient catalyst for oxygen evolution reaction. Nano Energy 30:267–275. https://doi.org/10.1016/j.nanoen.2016.10.020
26. Wu J et al (2022) Identifying and interpreting geometric Configuration-Dependent activity of spinel catalysts for water reduction. J Am Chem Soc 144:19163–19172. https://doi.org/10.1021/jacs.2c08726
27. Wang L-P, Van Voorhis T, Direct-Coupling O (2011) 2 bond forming a pathway in Cobalt oxide water oxidation catalysts. J Phys Chem Lett 2:2200–2204. https://doi.org/10.1021/jz201021n
28. Cao L et al (2019) Dynamic oxygen adsorption on single-atomic ruthenium catalyst with high performance for acidic oxygen evolution reaction. Nat Commun 10:4849. https://doi.org/10.1038/s41467-019-12886-z
29. Lu Z et al (2014) Electrochemical tuning of layered lithium transition metal oxides for improvement of oxygen evolution reaction. Nat Commun 5:4345. https://doi.org/10.1038/ncomms5345
30. Huang J et al (2025) Oxidation of interfacial Cobalt controls the pH dependence of the oxygen evolution reaction. Nat Chem 17:856–864. https://doi.org/10.1038/s41557-025-01784-1
31. Chong L et al (2023) La- and Mn-doped Cobalt spinel oxygen evolution catalyst for proton exchange membrane electrolysis. Science 380:609–616. https://doi.org/10.1126/science.ade1499
32. Priamushko T et al (2025) Be aware of transient dissolution processes in Co3O4 acidic oxygen evolution reaction electrocatalysts. J Am Chem Soc 147:3517–3528. https://doi.org/10.1021/jacs.4c14952
33. Rivas-Murias B, Salgueiriño V (2017) Thermodynamic CoO–Co3O4 crossover using Raman spectroscopy in magnetic octahedron-shaped nanocrystals. J Raman Spectrosc 48:837–841. https://doi.org/10.1002/jrs.5129
34. Hadjiev VG, Iliev MN, Vergilov IV (1988) The Raman spectra of Co3O4. J Phys C: Solid State Phys 21. https://doi.org/10.1088/0022-3719/21/7/007

35. Chuang TJ, Brundle CR, Rice DW (1976) Interpretation of the x-ray photoemission spectra of Cobalt oxides and Cobalt oxide surfaces. Surf Sci 59:413–429. https://doi.org/10.1016/0039-6028(76)90026-1
36. Morgan DJ (2015) Resolving ruthenium: XPS studies of common ruthenium materials. Surf Interface Anal 47:1072–1079. https://doi.org/10.1002/sia.5852
37. Jing C et al (2022) Electrocatalyst with dynamic formation of the dual-Active site from the dual pathway observed by in situ Raman spectroscopy. ACS Catal 12:10276–10284. https://doi.org/10.1021/acscatal.2c01038
38. Moysiadou A, Lee S, Hsu C-S, Chen HM, Hu X (2020) Mechanism of oxygen evolution catalyzed by Cobalt oxyhydroxide: Cobalt superoxide species as a key intermediate and dioxygen release as a Rate-Determining step. J Am Chem Soc 142:11901–11914. https://doi.org/10.1021/jacs.0c04867
39. Ram R et al (2024) Water-hydroxide trapping in Cobalt tungstate for proton exchange membrane water electrolysis. Science 384:1373–1380. https://doi.org/10.1126/science.adk9849

Publisher's Note